

Pressure fluctuations in turbulent flows over superhydrophobic surfaces

By J. Seo, R. García-Mayoral AND A. Mani

1. Motivation and objectives

The reduction of skin friction in turbulent flows has been an active area of research for several decades, and different strategies have been proposed and studied with mixed success. Of these, superhydrophobic surfaces for naval applications have received a great deal of attention recently. Superhydrophobicity enables textured surfaces immersed in water to entrap pockets (or bubbles) of air. The bubbles can lodge within the texture grooves, when the groove size is small enough. This is known as the Cassie-Baxter state (Cassie & Baxter 1944), in opposition to the fully-wetted, Wenzel state (Wenzel 1936), in which the surface cavities are filled with water and the hydrophobic effect is lost. Under Cassie-Baxter conditions, much of the overlying water flow is in contact with the entrapped air, and not with the solid surface. Thus, the air ‘layer’ acts as a lubricant for the outer flow, which can effectively slip over the wall, experiencing reduced friction compared to conventional, smooth surfaces (Rothstein 2010). The drag-reducing properties of superhydrophobic surfaces were first demonstrated for laminar flows (Watanabe *et al.* 1999; Ou *et al.* 2004; Choi & Kim 2006; Choi *et al.* 2006). Under turbulent conditions, Ou & Rothstein (2005) showed experimentally that superhydrophobic surfaces were able to achieve high drag reductions of up to at least 25%. Min & Kim (2005*a*) studied the reduction for turbulent flows numerically, modeling the superhydrophobicity of the surface as a uniform slip length. They also studied the effect of these surfaces on the stability of the flow and the transition to turbulence (Min & Kim 2005*b*). The assumption of a single, homogeneous slip length of Min & Kim (2005*a*), analogous to the nanoscale Navier-slip effect of hydrophobicity (Thompson & Troian 1997; Freund 2003), implies that the surface texture modeled is isotropic. More recently, Busse & Sandham (2012) proposed different streamwise and spanwise slip lengths to account for texture anisotropy. The detailed geometry of the texture was first studied in simulations by Martell *et al.* (2009), who used a patterned slip/no-slip boundary condition to model the alternating contact with the entrapped air pockets and the roughness crests separating them.

Although the drag-reducing properties of superhydrophobic surfaces on turbulent flows have received a great deal of attention recently, both experimentally (Ou & Rothstein 2005; Gogte *et al.* 2005; Daniello *et al.* 2009) and numerically (Min & Kim 2005*a*; Martell *et al.* 2009, 2010; Park *et al.* 2013), the interaction of these surfaces with the flow has not yet been fully understood. The above cited numerical studies have, for instance, concentrated on the drag-reducing slip effect, without considering the problem of gas-liquid interface stability and bubble depletion. The reduction predicted by these studies increases with the size of the texture grooves, in agreement with the theoretical analyses of Lauga & Stone (2003), Fukagata *et al.* (2006), and Ybert *et al.* (2007). In real flows, however, the superhydrophobic effect is completely lost for sufficiently large grooves, when the Cassie-Baxter state is lost and the surface is fully wetted (Aljallis *et al.* 2013).

Progress is currently being made on the fabrication of hierarchical (Lee & Kim 2011*b,a*) and gas-pocket-restoring (Lee & Kim 2012) surfaces to minimize dewetting effects.

In the present paper, we analyze possible degrading effects leading to the departure from the improving-with-size behavior just described. Some work in this direction is beginning to appear, but the mechanisms implicated in the degradation are still largely unknown. In particular, we focus on how pressure fluctuations are modified by the presence of superhydrophobic surfaces, since large local pressures will lead to bubble depletion. The deformation of the air pockets, and its interaction with the overlying turbulence, are currently under study by our group, and even though results are not yet available, we will describe the method developed to solve the coupling between pressure fluctuations and deformation at the interface. In the simulations cited previously of Martell *et al.* (2009, 2010), Min & Kim (2005*a*), and Park *et al.* (2013), it was assumed that the interface maintained a rigid, flat shape, so the wall-normal velocity was zero at the boundary surface. Instead, we model the surface deformation assuming that, under pressure fluctuations, the interface is able to deform following a Young-Laplace equation. We introduce the effect of the deformation on the overlying turbulent flow as a linearized boundary condition for the wall-normal velocity. Our work lines up with that of Hyväluoma & Harting (2008), Lee & Kim (2009), Teo & Khoo (2010), Patankar (2010), Samaha *et al.* (2011), Aljallis *et al.* (2013), and Busse & Sandham (2013), all studying possible degrading effects in superhydrophobic drag reduction. Busse & Sandham (2013) analyzed how the performance degrades as the air layer is lost and the texture crests begin to protrude out of it, introducing a roughness-like effect. Hyväluoma & Harting (2008) and Teo & Khoo (2010) considered the effect of stationary interface curvature. Lee & Kim (2009), Patankar (2010), and Samaha *et al.* (2011) analyzed the transition from the Cassie-Baxter to the Wenzel state through static pressure effects. Aljallis *et al.* (2013) considered the effect of shear on bubble depletion at high Reynolds numbers.

This paper is organized as follows. In Section 2 we present the equations for the problem and discuss the key dimensions and dimensionless parameters chosen for our simulations. In Section 3 we outline the numerical method used to solve that set of equations. Preliminary results for infinitely rigid air-water interfaces are presented and analyzed in Section 4. Finally, the conclusions are summarized in Section 5.

2. Problem formulation

Consider the motion of a turbulent liquid flow in a channel with superhydrophobic rough walls that have entrapped gas pockets, as sketched in Figure 1. The roughness is made up by a doubly-periodic patterned texture of characteristic size λ . We assume that the flow is governed by the incompressible Navier–Stokes equations,

$$\nabla \cdot \mathbf{u} = 0, \quad (2.1)$$

$$\frac{\partial \mathbf{u}}{\partial t} + \mathbf{u} \cdot \nabla \mathbf{u} = -\nabla p + \nu \nabla^2 \mathbf{u}, \quad (2.2)$$

where ν is the kinematic viscosity and the liquid density is $\rho = 1$.

The flow is bounded by protruding roughness elements and the gas pockets interspersed between them. No-slip is assumed at the solid-liquid interfaces, and free slip at the gas-liquid ones. All the boundaries are impermeable, but, while the solid-liquid ones are considered to be rigid, the gas-liquid ones deform in response to the local instantaneous

pressure jump across, $P_{gas} - P_{liquid}$, obeying to the Young-Laplace equation,

$$\nabla^2 \eta \approx \frac{P_{liquid} - P_{gas}}{\sigma}, \quad (2.3)$$

where σ is the surface tension and η the interface height. The rough elements are assumed to have flat crests with infinitely sharp edges, so that the gas-liquid interface is effectively pinned to those edges. We neglect the gas dynamics within the pockets, assuming that P_{gas} is uniform and that the mass of gas is preserved.

Under those conditions, the dimensional analysis of the problem produces a number of dimensionless parameters. The first is a Reynolds number based on the channel half-height, for instance the friction Reynolds number $Re_\tau = u_\tau \delta / \nu$, that measures how ‘turbulent’ the flow is. For a realistic naval application with a moving body of meter-scale length and a velocity of order ~ 5 m/s, Re_τ is typically ~ 4000 . This value is at present barely reachable by direct numerical simulation (Lee *et al.* 2012), so we run our simulations at a more modest $Re_\tau = 395$, at which near-wall effects can still be correctly simulated (García-Mayoral & Jiménez 2012). Another important Reynolds number is the size of the texture in viscous units $\lambda^+ = u_\tau \lambda / \nu$, which measures how much the flow deviates from a canonical, smooth-wall flow. For small λ^+ , the effect of the superhydrophobic surface can be treated as a perturbation for the turbulent flow, while for large λ^+ the flow is completely modified and resembles more a flow around obstacles. Typical experimental values are $\lambda^+ \approx 2-4$, but, because of computational realizability, we have run our simulations with $\lambda^+ \approx 150$. This value produces unrealistically large slip velocities and drag reductions, but it is of the same order of the state-of-the-art simulations with patterned textured surfaces (Martell *et al.* 2009, 2010), and we consider it sufficient for the present, preliminary simulations. Nonetheless, the discrepancy with realistic λ^+ values has to be taken into account when analyzing the results. The last key dimensionless number is a Weber number, which measures the relative importance of the surface tension. Using inner scaling, the Weber number could be defined as $We^+ = \rho u_\tau \nu / \sigma$. We^+ is appropriate to dimension problems for which variations of the interface height η occur for wall-parallel lengths determined by the turbulent pressure fluctuations, $\sim 200\nu/u_\tau$ (García-Mayoral & Jiménez 2012). On the other hand, if the surface texture wavelength λ is smaller than those $\sim 200\nu/u_\tau$, the length scale of η -variations is determined by λ . In this limit, a more suitable dimensionless number is $We = \rho u_\tau^2 \lambda / \sigma$. In our simulations both Weber numbers are equally significant, but matching the latter with that of practical applications, with smaller λ^+ , is more relevant from a technological perspective. We therefore have conducted our simulations at $We = 5 \times 10^{-3}$, similar to the typical values of practical applications. This implies that the interfaces in our simulations have a ‘deformability’ comparable to those of practical applications with $\lambda^+ \sim 5$, whereas in real flows with $\lambda^+ \sim 150$ interfaces would be much more flexible. Additionally, it will be shown in Section 4 that, for post configurations, there are stationary pressure distributions with the lengthscale of the texture, λ , which do not scale with ρu_τ^2 , but with ρU_{slip}^2 , where U_{slip} is the effective mean slip velocity at $y = 0$. The appropriate Weber number for the resulting, stationary interface deformation is therefore $\rho U_{slip}^2 \lambda / \sigma$. Although this effect is important in the simulations with posts, it can be expected to decrease for smaller λ^+ , since U_{slip} is roughly proportional to λ .

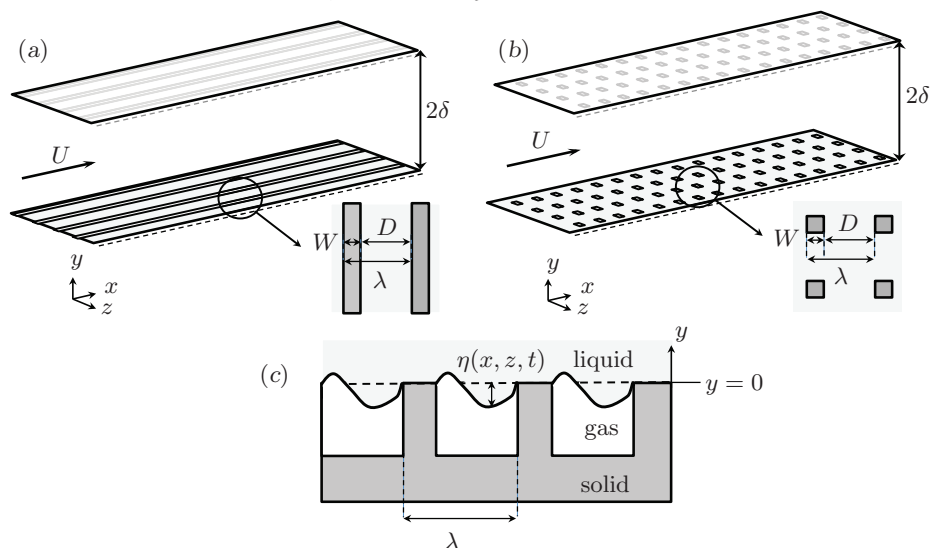


FIGURE 1. Schematic representation of a channel with superhydrophobic-surface boundary conditions on both walls, (a) streamwise-aligned ridges and (b) posts. W is the no-slip obstacle width, D the distance between obstacles, and $\lambda = W + D$ the wavelength of the pattern. Note that these representations do not exactly portray the arrangements studied, which have more texture features in the simulation domain than shown here. (c) Sketch illustrating the deformation of the gas-liquid interface, η .

3. Numerical method

The three-dimensional Navier-Stokes equations are discretized and solved computationally with the code of Bose *et al.* (2010), adapted to treat superhydrophobic textured boundaries. We use a second-order finite-difference scheme on a staggered mesh (Morinishi *et al.* 1998). The grid is Cartesian with uniform spacing in the streamwise (x) and spanwise (z) directions, and stretching in the wall-normal (y) direction. The computational domain is a periodic channel of ratio length–width–height of $2\pi \times \pi \times 2$, standard for simulations that focus on near-wall effects (Martell *et al.* 2009, 2010; García-Mayoral & Jiménez 2012), with $256 \times 256 \times 192$ points. All the simulations are conducted at $\text{Re}_\tau \approx 395$, resulting in a grid resolution $\Delta x^+ = 9.7, \Delta z^+ = 4.8, \min(\Delta y^+) = 0.15, \max(\Delta y^+) = 12$. The ‘+’ superscript denotes conventional wall-unit scaling with the friction velocity u_τ and the kinematic viscosity ν . The time discretization uses a second-order Adams-Bashforth scheme for the non-linear and wall-parallel diffusion terms, and a second-order Crank-Nicholson scheme for the wall-normal diffusion terms. Incompressibility is imposed through a fractional step implementation (Kim & Moin 1985). The flow is driven by a time-constant mean pressure gradient.

All simulations use symmetric channels, with both walls being either smooth or superhydrophobic. In the latter case, the gas-liquid interface is modeled as a perfect-slip boundary condition, resulting in a pattern of slip and no-slip conditions (Martell *et al.* 2009). We study the patterns sketched in Figures 1(a), posts distributed uniformly in the streamwise (x) and spanwise (z) directions, and 1(b), streamwise-aligned ridges. Spanwise-aligned ridges are less efficient for drag reduction than streamwise-aligned ones (Min & Kim 2005a; Martell *et al.* 2009; Choi *et al.* 2006), so we have left them out of our study. We select an equal pattern wavelength $\lambda^+ = W^+ + D^+ \approx 155$ for both ridge

Case	Surface type	λ^+	w^+	We	U_{slip}^+	$P'^+(y=0)$	$\bar{P}_{0,rms}^+$	$p'_{0,rms}^+$
S	Smooth	n.a.	n.a.	0	0	2.1	0.1	2.1
P _{ND}	Posts	155.1	38.8	0	27	8.8	8.1	3.1
R _{ND}	Ridges	155.1	19.4	0	31	4.1	0.5	4.1

TABLE 1. Simulation parameters. λ^+ and w^+ are the pattern wavelength and thickness. $We = \rho u_\tau^2 \lambda / \sigma$ is the Weber number, and U_{slip}^+ the mean slip velocity. P'^+ , $\bar{P}_{0,rms}^+$ and $p'_{0,rms}^+$ are the total, stationary and time-dependent pressure rms fluctuations at $y = 0$.

and post configurations. The pattern thickness W^+ has been adjusted to obtain comparable slip velocities for both configurations. For posts, we use $W^+ \approx 40$, and for ridges $W^+ \approx 20$, resulting in gas fractions 1/16 and 1/8, respectively.

For the first time in the literature, the effect of the deformation of the gas-liquid interface in response to the overlying turbulent flow is studied in our simulations. We define η as the interface height measured from the plane that contains the flat, no-slip crests of the roughness elements, $y^+ = 0$, as sketched in Figure 1(c). We assume that η is small, and treat its deformation as a linearized boundary condition for the wall-normal velocity at the virtual boundary plane $y^+ = 0$. The deformation responds to the pressure difference across the interface, obeying the Young-Laplace equation (2.3). Within the gas pockets, P_{gas} is assumed to be uniform, and is determined by the mass conservation of the gas, so that at all times

$$\iint \eta \, dx \, dz = 0. \quad (3.1)$$

The above integral condition implicitly assumes that the interface is initially located at $y = 0$, that it never breaks, and that the Cassie-Baxter state is always preserved. At the liquid-solid interface, η is always zero. The motion of the interface generates a non-zero wall-normal velocity at the interface,

$$v(x, y = \eta, z) = \frac{D\eta}{Dt} = \frac{\partial\eta}{\partial t} + u \frac{\partial\eta}{\partial x} + w \frac{\partial\eta}{\partial z}. \quad (3.2)$$

The Taylor expansion of Eq. (3.2) around $y = 0$, combined with the continuity equation, leads to

$$v(x, y = 0, z) = \frac{\partial\eta}{\partial t} + \frac{\partial(\eta u)}{\partial x} + \frac{\partial(\eta w)}{\partial z}. \quad (3.3)$$

This non-zero wall-normal velocity is imposed as a boundary condition for the turbulent flow of the overlying liquid. Note that Eq. (2.3) couples this boundary condition with the pressure in the flow. We solve this coupling explicitly, with a small enough time step to guarantee the stability of the time integration.

The simulations are conducted with a constant Courant-Friedrichs-Lewy number CFL = 0.25, so that the variable time step is determined by

$$\Delta t = \text{CFL} \times \left(\max \left\{ \frac{|u|}{2\Delta x} + \frac{|v|}{2\Delta y} + \frac{|w|}{2\Delta z} + \frac{4}{\text{Re}\Delta x^2} + \frac{4}{\text{Re}\Delta z^2} \right\} \right)^{-1}. \quad (3.4)$$

The simulations were run for at least 35 largest-eddy-turnover times δ/u_τ , of which the first 10 were discarded for statistical sampling, to avoid any contamination from initial transients.

The set of simulations conducted is summarized in Table 1, where the geometry of the

surface pattern, the interface deformability, and some key statistical results are included. The code has been validated with the turbulent, smooth-wall channel at $Re_\tau \approx 395$ of Moser *et al.* (1998), and that with streamwise ridges of size $w^+ = g^+ \approx 74$ and $w^+ = g^+ \approx 37$, also at $Re_\tau \approx 395$, from Martell *et al.* (2010).

4. Results and discussion

In this section, the turbulent statistics resulting from our simulations at $We = 0$ for each geometric configuration are presented and analyzed. Because of their impact on the deformation and stability of the gas-liquid interface, the pressure fluctuations are given special attention.

Mean streamwise velocity profiles $U(y)$ are portrayed in Figure 2, illustrating how the superhydrophobic surfaces produce large U_{slip} values, which have in turn a large impact on the bulk velocity. The $U(y)$ profiles for the cases with interface deformation, not presented here, are nearly identical to those with deformation. The post configuration yields $U_{slip}^+ = 27$, while ridges produce a larger $U_{slip}^+ = 31$. Because of the large $\lambda^+ \approx 155$, these values are comparable to the centerline velocity of the smooth channel flow. It could be expected that such large values do not merely shift the mean U profile, yet its shape is only modified below $y^+ \approx 50$, as shown in Figure 2(b). The velocity fluctuations are also very similar when compared to the smooth-wall case, with the exception of the aforementioned near-wall region, $y^+ \lesssim 50$, where fluctuations over superhydrophobic surfaces are significantly larger, as illustrated in Figure 3. Once more, the differences between deformable and non-deformable gas-liquid interfaces, not portrayed, are small. The streamwise rms fluctuation, u'^+ , has a high peak at $y^+ = 0$ of order 10-12 wall units, produced by the large in-plane variation of u^+ , which averages $U_{slip}^+ = 27 - 31$ but is at the same time zero over the no-slip obstacles. Although not as high as the u'^+ peak, the spanwise rms is also significant. This is due to the secondary lateral motions and the relative freedom that they have to slip at the $y^+ = 0$ plane. Even v'^+ , which at the boundary plane is zero for rigid surfaces –and very small for deformable interfaces, experiences a significant increase in the immediate vicinity of the wall. A similar behavior is observed for the uv Reynolds stress. We do not observe the reduction in the peak fluctuations reported by Martell *et al.* (2009) over superhydrophobic surfaces, although we did indeed observe it in the validation case that repeated their setup. This is likely an effect of their asymmetrical setup, with one smooth and one superhydrophobic wall. As one wall experiences a higher shear than the other, their friction velocities are different, and even the definition of δ for each wall becomes ambiguous, as the center line is no longer a symmetry axis. Under those conditions, dimensioning the results correctly can be challenging. This is the main reason for our choice of symmetric channels.

More interesting is the effect of superhydrophobic surfaces on the pressure fluctuations. Figure 4 shows that the values of $P'(y)$ away from the wall do not vary noticeably from those over smooth walls. At the same time, significant differences can be observed near the wall, particularly for the uniformly-distributed posts. For the post case, the near-wall fluctuations, $P'^+ \approx 9$, are much higher than for ridges and smooth walls, $P'^+ \approx 2 - 4$. To analyze the large P'^+ values at $y^+ = 0$, we have examined instantaneous realizations of the pressure distribution at that plane. Examples are portrayed in Figure 5. Examination reveals that the large pressure variations are associated with the geometric distribution of the no-slip patterns. High pressure zones appear in front of posts, where the slipping flow is forced to halt or divert into v and w momentum, as discussed in the previous paragraph,

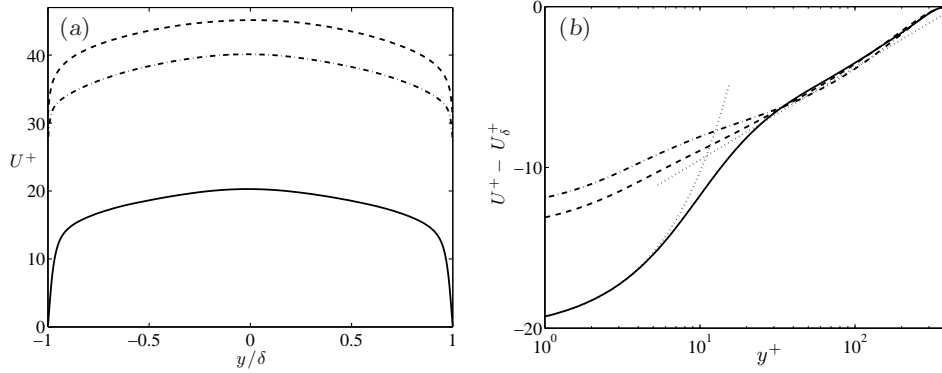


FIGURE 2. (a) Mean streamwise velocity profile in linear scale and (b) velocity defect law in logarithmic scale. —, smooth channel; ---, post; - · - ·, ridges; · · · · ·, predictions from theory for the viscous and logarithmic regions, $U^+ = y^+$ and $U^+ = 0.41^{-1} \log(y^+) + 5.0$.

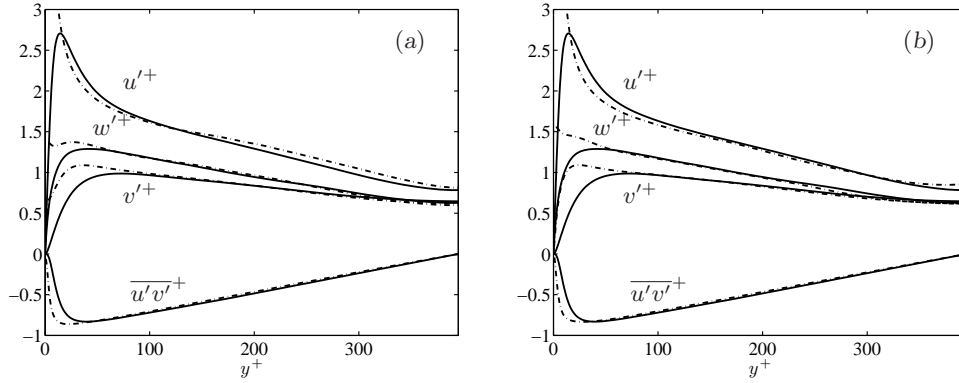


FIGURE 3. Velocity fluctuations, u'^+ , v'^+ , w'^+ and Reynolds stress $\overline{u'v'^+}$ for superhydrophobic surfaces with (a) posts and (b) ridges at $Re_\tau \approx 395$. - · - ·, superhydrophobic walls with $We = 0$; —, smooth channel.

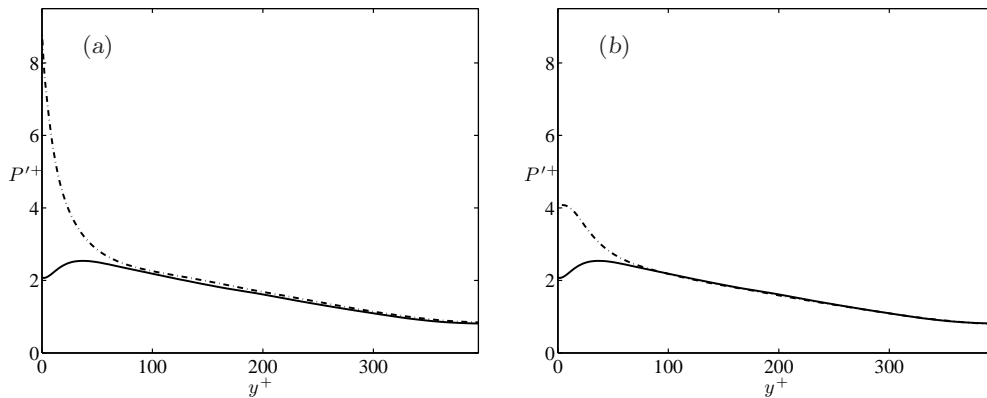


FIGURE 4. Pressure fluctuation profiles for superhydrophobic surfaces with (a) posts and (b) ridges at $Re_\tau \approx 395$. - · - ·, superhydrophobic walls with $We = 0$; —, smooth channel.

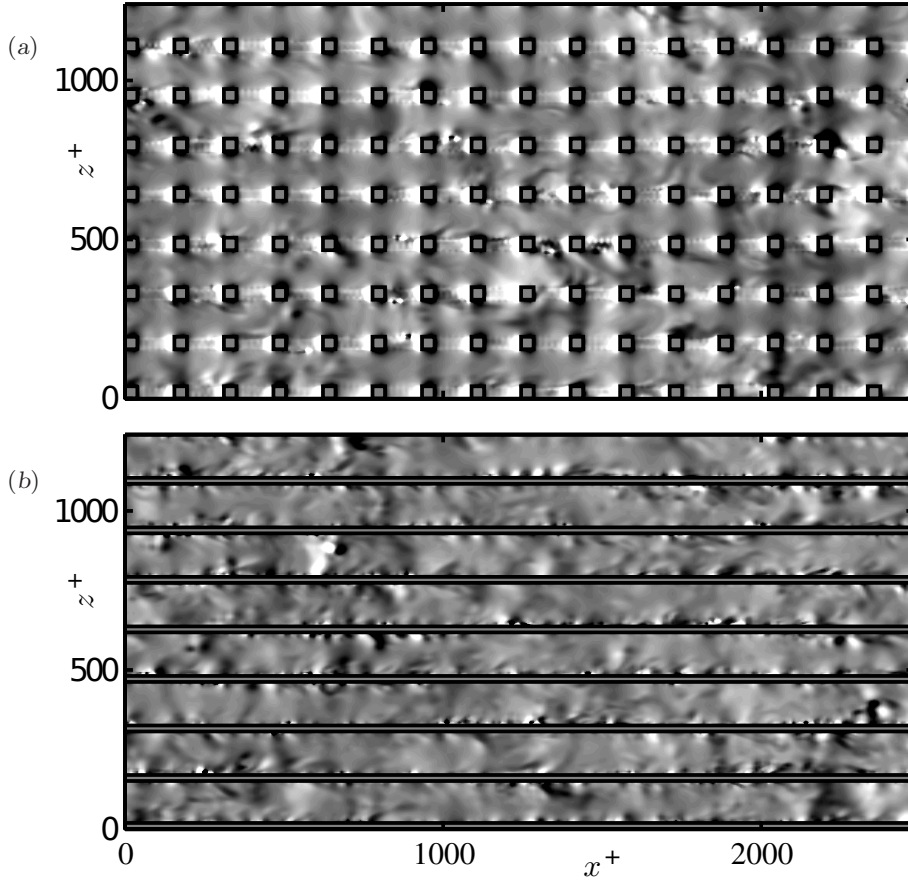


FIGURE 5. Comparison of instantaneous pressure contours at the $y = 0$ plane, for (a) case P_{ND} and (b) case R_{ND} . From dark to clear, pressure fluctuations range between -10 and 10 wall units.

forming stationary stagnation regions. The maximum pressure in these regions reaches values as high as $P_{max}^+ \approx 60$. In the case of ridges, these stationary stagnation regions do not exist, and the typical values of the pressure at $y^+ = 0$ are much closer to the smooth-wall values.

Besides the stationary component, there is a smaller, time-fluctuating one, which resembles closely the behavior of the fluctuations for smooth walls. This resemblance can be quantified by decomposing the pressure fluctuations at $y^+ = 0$ into the time-averaged, stationary term, \bar{P}_0 , and a time-and-space-dependent fluctuation p'_0 ,

$$P(x, y = 0, z, t) = \bar{P}_0(x, z) + p'_0(x, z, t), \quad (4.1)$$

where

$$\bar{P}_0(x, z) = \langle P(x, y = 0, z, t) \rangle_t, \quad (4.2)$$

and define $p'_{0,rms}$ and $\bar{P}_{0,rms}$ as the root mean square values of p'_0 and \bar{P}_0 , respectively. While p'_0 can be interpreted as the pressure component produced by the overlying tur-

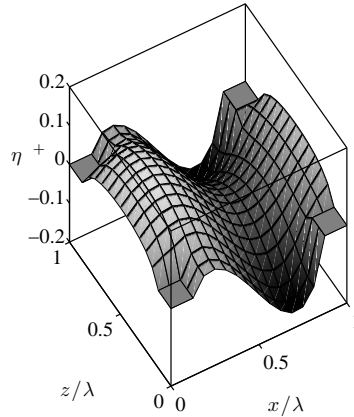


FIGURE 6. Interface deformation $\langle \eta^+ \rangle_t$ in a periodic unit of surface texture, derived from the time-averaged pressure pattern generated by the stagnation mechanism in case P_{ND} . Note that only one quarter of each post is shown at the corners.

bulent flow, \bar{P}_0 is a ‘form’ pressure produced by the geometric arrangement of the no-slip obstacles.

Table 1 includes values of $P'^+(y=0)$, $p'_{0,\text{rms}}$ and $\bar{P}_{0,\text{rms}}^+$ for our simulations. The results show that, for case R_{ND} , $p'_{0,\text{rms}}$ and $P'^+(y=0)$ are essentially equal. Since the ridges are aligned with the flow direction, there are no stationary stagnation regions, and the pressure fluctuations are mainly caused by the overlying turbulent flow. The difference comes from the small contribution caused by the secondary cross-flow stagnating at the sides of the ridges, but that effect is not stationary and cannot be easily separated from the turbulent contribution, although the two-dimensional spectral distribution of the fluctuations should reveal its clear footprint for spanwise wavelengths λ^+ , D^+ , and W^+ . On the other hand, the high $P'_{0,\text{rms}}$ in case P_{ND} implies that most of the high value of P' near walls with posts is not related to turbulence, but to the form drag generated by the posts (which should also show a clear footprint in the spectrum at wavelengths λ^+ , D^+ , and W^+).

The pressure distribution at the wall would be coupled with the interface shape η through Eq. (2.3)–(3.1). The interface would be pushed downward in front of posts, where the pressure is higher, and upwards right behind the posts, where the pressure is lower. The time-averaged interface shape, produced by \bar{P}_0 , is portrayed in Figure 6 in a periodic-pattern unit, as it would be for $We = 5 \times 10^{-3}$. Note that the maximum interface deformation is of order $\eta^+ \approx 0.1$. The corresponding induced v_s^+ would also be of order 0.1, justifying the use of linearized boundary conditions for future simulations allowing gas-liquid interfaces to deform.

In the case of posts, the large values of \bar{P}_0^+ for large λ^+ impose a practical limit for the texture size, since excessively large pressures will lead to the depletion of gas pockets. Note that we have obtained small η -displacements because we are matching the Weber number that would characterize air-water interfaces of size $\lambda^+ \approx 4$ in a realistic case. For $\lambda^+ \approx 150$, the flexibility of an air-water interface would be roughly 40 times larger than in our simulations. The η -displacements would then be between one and two orders of magnitude larger, leading to the breakup of the entrapped air bubbles. At the same time, drag reduction increases with λ^+ (Rothstein 2010), so it is desirable to design textures as

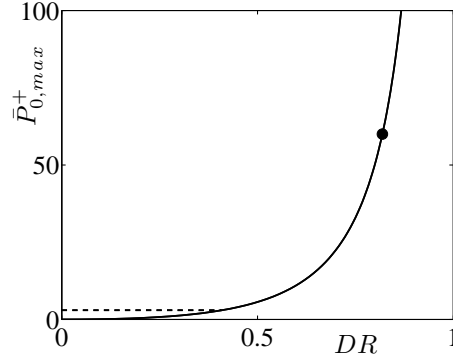


FIGURE 7. —, theoretical evolution of the maximum of the stationary component of the pressure at the gas-liquid interface with the drag reduction. The symbol corresponds to the values of case P_{ND} ; ----, typical turbulent pressure fluctuation at the wall in a smooth channel, $p'_{max}^+ \approx 3$.

large as possible. The relative drag reduction, DR , compared to the smooth wall under the same mean pressure gradient, can be expressed as

$$DR = \frac{\Delta C_f}{C_{f0}} = 1 - \frac{U_b^2}{(U_b + U_{slip})^2}, \quad (4.3)$$

where C_{f0} is the friction coefficient and U_b the bulk velocity for the smooth case. The benefit of a large U_{slip} , which is roughly proportional to λ^+ , is evident in the equation. On the other hand, the stationary component of the pressure, \bar{P}_0^+ , scales as

$$\bar{P}_0^+ \propto \rho U_{slip}^{+2}. \quad (4.4)$$

This implies that larger DR comes at the cost of higher pressures in front of the posts. The relationship between the maximum \bar{P}_0^+ and DR , as derived from Eq. (4.3) and (4.4), is portrayed in Figure 7. The free constant that Eq. (4.4) leaves has been set using the values of $\bar{P}_{0,max}^+$ and DR for case P_{ND} , so the curve can only be considered for rough estimates. For $DR \lesssim 50\%$, the stagnation effect produces maximum pressures comparable to typical turbulent fluctuations, but $\bar{P}_{0,max}^+$ increases rapidly for larger DR . In order to achieve larger reductions, ridge configurations without stationary stagnation regions should be favored.

As discussed above, the stationary pressure component can be expected to decrease rapidly for smaller, more realistic λ^+ surface patterns. The dominating term would then be the turbulent p'_0^+ . As shown in Table 1, if the interface deformation is not considered, the value of p'_0^+ is close to that of $P'^+(y=0)$ for smooth walls. It remains to be seen whether the simulations that consider the effect of the interface deformation result in similar values of p'_0^+ .

5. Concluding remarks

In the present work, we have studied the dynamics of turbulent flows over superhydrophobic, textured walls with entrapped pockets of gas. As the liquid slips over the gas pockets, the friction is reduced compared to conventional, smooth walls. The reduction predicted by previous studies increases with the size of the features in the texture, scaled

in wall units. However, very large features will eventually lead to the instability of the entrapped gas pockets and their depletion. To investigate the deleterious effects eventually leading to that depletion, we have investigated how superhydrophobic surfaces affect pressure fluctuations. We have conducted a series of direct numerical simulations of channels with two surface configurations, uniformly distributed posts and streamwise aligned ridges. Ridges and posts produce similar slip velocities when their sizes are comparable, and induce in the vicinity of the wall velocity fluctuations significantly larger than smooth walls. The most remarkable differences can, however, be found in the pressure statistics. A critical source of high pressures is the formation of stagnation regions in front of the protruding features of the solid wall, which act as obstacles. The resulting pressure values increase rapidly with texture size, effectively imposing a limit on the drag reduction that can be achieved using such configurations. One simple way to circumvent this problem is to design textures with streamwise aligned features, since these geometries are much less susceptible to the formation of stagnation regions. The ridge configuration studied is an example of such a geometry.

Acknowledgments

The authors would like to thank the Office of Naval Research for the support of this research under grant 3002451214 .

REFERENCES

- ALJALLIS, E., SARSHAR, M. A., DATLA, R., SIKKA, V. & JONE, A. 2013 Experimental study of skin friction drag reduction on superhydrophobic flat plates in high Reynolds number boundary layer flow. *Phys. Fluids* **25**, 025103.
- BOSE, S. T., MOIN, P. & YOU, D. 2010 Grid-independent large-eddy simulation using explicit filtering. *Phys. Fluids* **22**, 105103.
- BUSSE, A. & SANDHAM, N. D. 2012 Influence of an anisotropic slip-length boundary condition on turbulent channel flow. *Phys. Fluids* **24**, 055111.
- BUSSE, A. & SANDHAM, N. D. 2013 Turbulent flow over superhydrophobic surfaces - roughness versus slip. In *14TH European Turbulence Conference*. Lyon, France.
- CASSIE, A. B. D. & BAXTER, S. 1944 Wettability of porous surfaces. *Trans. Faraday Soc.* **40**, 546–551.
- CHOI, C.-H. & KIM, C.-J. 2006 Large slip of aqueous liquid flow over a nanoengineered superhydrophobic surface. *Phys. Rev. Lett.* **96**, 066001.
- CHOI, C.-H., ULMANELLA, U., KIM, J., HO, C.-M. & KIM, C.-J. 2006 Effective slip and friction reduction in nanograted superhydrophobic microchannels. *Phys. Fluids* **18**, 087105.
- DANIELLO, R., WATERHOUSE, N. E. & ROTHSTEIN, J. P. 2009 Turbulent drag reduction using superhydrophobic surfaces. *Phys. Fluids* **21**, 085103.
- FREUND, J. B. 2003 The atomic detail of a wetting/de-wetting flow. *Phys. Fluids* **15**, L33–36.
- FUKAGATA, K., KASAGI, N. & KOUMOUTSAKOS, P. 2006 A theoretical prediction of friction drag reduction in turbulent flow by superhydrophobic surfaces. *Phys. Fluids* **18**, 051703.
- GARCÍA-MAYORAL, R. & JIMÉNEZ, J. 2012 Scaling of turbulent structures in riblet channels up to $Re_\tau \approx 550$. *Phys. Fluids* **24**, 105101.

- GOGTE, S., VOROBIEFF, P., TRUESDELL, R., MAMMOLI, A., SWOL, F. V., SHAH, P. & BRINKER, C. J. 2005 Effective slip on textured superhydrophobic surfaces. *Phys. Fluids* **17**, 051701.
- HYVÄLUOMA, J. & HARTING, J. 2008 Slip flow over structured surfaces with entrapped microbubbles. *Phys. Rev. Lett.* **100**, 246001.
- KIM, J. & MOIN, P. 1985 Application of a fractional step method to incompressible Navier-Stokes equations. *J. Comput. Phys.* **59**, 308–323.
- LAUGA, J. & STONE, H. 2003 Effective slip in pressure-driven Stokes flow. *J. Fluid Mech.* **489**, 55–77.
- LEE, C. & KIM, C.-J. 2009 Maximizing the giant liquid slip on superhydrophobic microstructures by nanostructuring their sidewalls. *Langmuir* **25**, 12812–12818.
- LEE, C. & KIM, C.-J. 2011*a* Influence of surface hierarchy of superhydrophobic surfaces on liquid slip. *Langmuir* **27**, 4243–4248.
- LEE, C. & KIM, C.-J. 2011*b* Underwater restoration and retention of gases on superhydrophobic surfaces for drag reduction. *Phys. Rev. Lett.* **106**, 014502.
- LEE, C. & KIM, C.-J. 2012 Wetting and active dewetting processes of hierarchically constructed superhydrophobic surfaces fully immersed in water. *J. MEMS* **21**, 712–720.
- LEE, M., MALAYA, N. & MOSER, R. 2012 Direct numerical simulation for turbulent channel flow at high Reynolds number. In *Proc. 65th Annual Meeting of the APS Division of Fluid Dynamics*.
- MARTELL, M. B., PEROT, J. B. & ROTHSTEIN, J. P. 2009 Direct numerical simulations of turbulent flows over superhydrophobic surfaces. *J. Fluid Mech.* **620**, 31–41.
- MARTELL, M. B., ROTHSTEIN, J. P. & PEROT, J. B. 2010 An analysis of superhydrophobic turbulent drag reduction mechanisms using direct numerical simulation. *Phys. Fluids* **22**, 065102.
- MIN, T. & KIM, J. 2005*a* Effects of hydrophobic surface on skin-friction drag. *Phys. Fluids* **16**, L55–L58.
- MIN, T. & KIM, J. 2005*b* Effects of hydrophobic surface on stability and transition. *Phys. Fluids* **17**, 108106.
- MORINISHI, Y., LUND, T. S., VASILYEV, O. V. & MOIN, P. 1998 Fully conservative higher order finite difference schemes for incompressible flow. *J. Comput. Phys.* **143**, 90–124.
- MOSER, R., KIM, J. & MANSOUR, N. 1998 Direct numerical simulation of turbulent channel flow up to $re_\tau \approx 590$. *Phys. Fluids* **11**, 943–945.
- OU, J., PEROT, J. B. & ROTHSTEIN, J. P. 2004 Laminar drag reduction in microchannels using ultrahydrophobic surfaces. *Phys. Fluids* **16**, 4635–4643.
- OU, J. & ROTHSTEIN, J. P. 2005 Direct velocity measurements of the flow past drag-reducing ultrahydrophobic surfaces. *Phys. Fluids* **17**, 13606.
- PARK, H., PARK, H. & KIM, J. 2013 A numerical study of the effects of superhydrophobic surface on skin-friction drag in turbulent channel flow. *Phys. Fluids* **25**, 110815.
- PATANKAR, N. A. 2010 Consolidation of hydrophobic transition criteria by using an approximate energy minimization approach. *Langmuir* **26**, 8941–8945.
- ROTHSTEIN, J. P. 2010 Slip on superhydrophobic surfaces. *Annu. Rev. Fluid Mech.* **42**, 89–109.
- SAMAHA, M. A., VAHEDI, T. H. & EL HAK, M. G. 2011 Modeling drag reduction and

- meniscus stability of superhydrophobic surface of random roughness. *Phys. Fluids* **23**, 012001.
- TEO, C. J. & KHOO, B. C. 2010 Flow past superhydrophobic surfaces containing longitudinal grooves: effects of interface curvature. *Microfluidics and Nanofluidics* **9**, 499–511.
- THOMPSON, P. A. & TROIAN, S. M. 1997 A general boundary condition for liquid flow at solid surfaces. *Nature* **389**, 360–362.
- WATANABE, K., YANUAR & UDAGAWA, H. 1999 Drag reduction of newtonian fluid in a circular pipe with highly water-repellent wall. *J. Fluid Mech.* **381**, 225–238.
- WENZEL, R. N. 1936 Resistance of solid surfaces to wetting by water. *Ind. Eng. Chem.* **28**, 988–994.
- YBERT, C., BARENTIN, C. & COTTIN-BIZONNE, C. 2007 Achieving large slip with superhydrophobic surfaces: Scaling laws for generic geometries. *Phys. Fluids* **19**, 123601.